PAPER

Synergistic boron-based nanocrystal and amorphous Ni–Fe–B catalyst for high-performance flexible zinc-air batteries

Sai Li,[*a] Shuoshuo Wang,[a] Qinqin Chen,[b] Dongyuan Yang,[a] Yuhang Wang,[a] Haixia Wu,[a] Yameng Ma,[a] Zekai Ma,[a] Qi Chen,[a] Jiahao Zhouhuang,[a] Qiuliang Yu,[c] Lihui Zeng,[d] Haiyan Zhu,[e] Peng Ren,[f] Qing Feng,[*f] Rui Tan [iD][g] and Zhiming Feng [iD][*h]

Flexible zinc-air batteries (FZABs) are still limited by slow oxygen electrocatalysis and poor mechanical durability. In this work, we prepare a Ni–Fe–B catalyst with a nanocrystalline–amorphous composite structure through a two-step chemical reduction method. The amorphous Ni–B matrix stabilizes uniformly dispersed Fe nanocrystals, generating abundant unsaturated coordination sites and forming a mesoporous network (2–6 nm) that promotes the accessibility of active sites and facilitates mass transport. Boron-mediated electronic interaction between Ni and Fe modulates the surface electronic states, which lowers the interfacial charge-transfer resistance to 3–5 Ω cm^2 and improves the oxygen reduction reaction (ORR) activity, yielding a half-wave potential of 0.86 V *vs.* RHE, comparable to that of commercial Pt/C. When applied as the cathode in FZABs, this catalyst exhibits a peak power density of 224.9 mW cm^{-2} and remarkable cycling stability, with a voltage decay rate of only 0.05 mV h^{-1} over 100 h. The assembled battery also retains stable output under repeated bending between 0° and 180°, showing voltage fluctuations within 50 mV, thereby confirming excellent mechanical tolerance. This study demonstrates for the first time the use of bimetallic borides in FZABs and proposes a material design strategy that combines an amorphous host, a mesoporous structure, and bimetallic synergy to achieve high-performance, deformable zinc-air battery systems.

Introduction

Achieving global net-zero carbon emissions and mitigating climate change require transformative advances in renewable energy generation and storage technologies.[1–4] With the rapid expansion of solar, wind, and other intermittent energy sources, the demand for efficient and sustainable energy conversion and storage devices has become increasingly urgent.[5–11] Among the diverse strategies, rechargeable batteries represent the fundamental energy supply units for

portable electronic devices, electric vehicles, and large-scale grid storage.[9,12–14] At the same time, electrochemical energy storage and conversion technologies enables the generation of value-added fuels and chemicals, thereby contributing to a sustainable circular carbon economy.[15–20] The continuous performance evolution of these technologies profoundly shapes the development trajectory of the new energy industry.[21–23] Within the family of rechargeable batteries, lithium-ion batteries (LIBs) have become the dominant technology owing to their high energy density and excellent cycling stability, and they are now widely adopted in consumer electronics, electric vehicles, and stationary power applications.[24] Nevertheless, LIBs suffer from three intrinsic limitations.[25] First, the extremely low crustal abundance of lithium (approximately 20 ppm) not only elevates raw material costs but also induces supply chain risks due to its uneven global distribution. Second, their theoretical energy density (300–400 W h kg^{-1}) remains insufficient to satisfy the ever-increasing demand for next-generation high-capacity storage, such as long-range electric vehicles and wearable electronics. Third, the use of organic electrolytes renders LIBs vulnerable to thermal runaway under elevated temperatures or

[a] *School of Chemistry and Chemical Engineering, Xi'an University of Science and Technology, Xi'an, 710054, China. E-mail: saili@xust.edu.cn*
[b] *Multidimensional Additive Manufacturing Institute, Faculty of Mechanical Engineering and Mechanics, Ningbo University, 315211, Ningbo, China*
[c] *Shaanxi Anchuang Electronic Technology Co., LTD, Xi'an, 710201, China*
[d] *Kaili Catalyst New Materials CO., LTD, Xi'an, 710201, China*
[e] *Shaanxi Key Laboratory for Theoretical Physics Frontiers, Institute of Modern Physics, Northwest University, Xi'an, Shaanxi 710069, China*
[f] *Xi'an Tai Jin Xin Neng Technology Co., LTD, Xi'an, 710201, China. E-mail: fengqing0715@126.com*
[g] *Department of Chemical Engineering, Swansea University, Swansea, SA1 8EN, UK*
[h] *Department of Chemical Engineering, University of Manchester, Manchester, M13 9PL, UK. E-mail: zhiming.feng@manchester.ac.uk*

This journal is © The Royal Society of Chemistry 2026

Catal. Sci. Technol., 2026, **16**, 1411–1420 | 1411

overcharging, leading to severe safety hazards including fire and explosion. Furthermore, although traditional secondary batteries such as lead-acid and nickel-metal hydride batteries are cost-effective, their energy densities remain considerably lower (e.g., lead-acid batteries only 30–50 W h kg^{-1}).[26] Additionally, the presence of heavy metals such as lead and cadmium in these batteries poses serious environmental concerns, further restricting their deployment in advanced energy applications.[27]

Zinc-air batteries (ZABs), as a representative type of metal-air battery, operate *via* the electrochemical reaction between a zinc anode and oxygen from ambient air. Their unique reaction mechanism endows them with performance advantages far superior to those of traditional secondary batteries. In terms of energy density, ZABs possess a theoretical value of up to 1086 W h kg^{-1} (based on zinc mass), which is more than three times that of LIBs. This effectively bridges the gap between high-capacity energy storage demands and current technologies. From a resource and cost perspective, zinc, the fourth most abundant metal in the Earth's crust with an abundance of approximately 70 ppm, is about fifty times less expensive than lithium and exhibits excellent environmental compatibility, thereby avoiding the heavy-metal pollution issues of conventional systems. With respect to safety, ZABs generally employ aqueous electrolytes (e.g., KOH solution), eliminating the flammability risks associated with organic electrolytes. Moreover, their wide operating temperature range (−20 to 60 °C) further enhances operational reliability. Collectively, these merits establish ZABs as a promising candidate to replace LIBs and accelerate the advancement of energy storage technologies. With the rapid development of wearable electronics (e.g., flexible smart bracelets and foldable smartphones), flexible robotics, and implantable medical devices, the flexibility of energy supply systems has become an essential technological requirement. Boride-based catalysts have been reported for conventional rigid ZABs.[28] However, to the best of our knowledge, there are no prior studies on the application of bimetallic borides in flexible zinc-air batteries (FZABs), where additional requirements such as mechanical flexibility, bending durability, and strong interfacial bonding with flexible substrates must be satisfied. This work therefore represents the first demonstration of bimetallic borides applied in FZABs, providing new insights into the design of cost-effective and mechanically robust catalysts for flexible energy storage devices. Building on the performance advantages of conventional ZABs, FZABs realize remarkable mechanical deformability through flexible electrode architectures and electrolyte systems, such as copper mesh current collectors and solid gel electrolytes, which enable them to endure repeated bending (0° to 180°), folding, and even stretching. They can conform intimately to flexible substrates, thereby effectively addressing the compatibility challenges between rigid batteries and flexible devices.[29] Furthermore, the solid or quasi-solid electrolytes employed in FZABs eliminate the leakage risks associated

with liquid electrolytes, thereby enhancing device portability and reliability. This renders them a promising energy solution for flexible electronics. However, the practical deployment of FZABs is still hindered by two fundamental challenges, both arising from performance bottlenecks at the air cathode. The first is the sluggish kinetics of the ORR. As the key cathodic process in FZABs, ORR proceeds through a four-electron transfer pathway. The high reaction energy barrier and sluggish kinetics give rise to substantial polarization losses, typically restricting the energy conversion efficiency to below 60%. The second challenge is inadequate mechanical durability. Under repeated bending and folding, flexible electrodes are susceptible to structural cracking, while the catalyst layer tends to delaminate from the current collector and electrolyte interfaces. These degradations lead to the loss of active sites and interruption of ion and electron transport pathways. After 100 h of cycling, the voltage decay rate often exceeds 0.1 mV h^{-1}, which falls far short of practical requirements.[30]

To address the above challenges in FZABs, extensive efforts have been devoted to the rational design of high-performance air cathode catalysts and flexible electrolytes.[31–36] Previous studies have investigated atomically dispersed multi-site catalysts for FZABs using heterostructure engineering, heteroatom regulation, and multi-metal synergy. However, issues related to mechanical stability, mass transport, and scalable synthesis remain to be addressed. Building on this concept of heterostructure engineering, Zhong *et al.*[37] prepared Fe$_3$C/MnO heterostructured nitrogen-doped carbon catalysts (Fe$_3$C/MnO-NC) by pyrolyzing FeMn bimetallic MOFs at 900 °C under argon. Combined with DFT calculations, they revealed interfacial electronic regulation mechanisms and further synthesized PAM–PAA–Gly composite gel electrolytes (GPE) to enhance ion transport. The Fe$_3$C/MnO interfaces optimized intermediate adsorption energy barriers, affording ORR $E_{1/2}$ = 0.86 V, OER overpotential = 349 mV (ΔE = 0.74 V). Liquid FZABs reached a peak power density of 157.8 mW cm^{-2}, and flexible devices cycled stably for 48 h. Nonetheless, limitations included a relatively low BET surface area (123.7 m^2 g^{-1}, restricting active-site exposure), high energy consumption from pyrolysis, and poor GPE ionic conductivity below −40 °C. Atomic-dispersion strategies have been widely explored to construct transition-metal-based catalysts using framework-derived precursors, composition regulation, and controlled pyrolysis to generate well-defined coordination environments. In parallel, low-cost and sustainable precursor routes and composite catalyst–electrolyte systems have been investigated to enhance active-site utilization and operational adaptability; however, challenges related to composition tolerance, long-term structural stability, uniformity in large-scale synthesis, and mechanistic verification remain. Zhang *et al.*[38] fabricated Co–N$_x$-enriched porous carbon nanofiber (Co–N$_x$/EPCF) catalysts by electrospinning PAN/Co(NO$_3$)$_2$/SiO$_2$ precursors, followed by carbonization at 900 °C and HF

1412 | *Catal. Sci. Technol.*, 2026, **16**, 1411–1420

This journal is © The Royal Society of Chemistry 2026

etching to remove SiO_2. The catalyst possessed a BET surface area of 300 m^2 g^{-1}, ORR $E_{1/2}$ = 0.82 V, and OER potential = 1.69 V at 10 mA cm^{-2} (ΔE = 0.87 V). Flexible FZABs based on this material cycled stably for 37 h, with voltage fluctuations <80 mV during 0–180° bending and good methanol tolerance. However, its Co content was only 0.09%, leading to a 15–20% voltage plateau drop at >20 mA cm^{-2}; electrospinning yield was low (<10 g h^{-1}), and PAM gel electrolytes exhibited limited ionic conductivity (11 mS cm^{-1}). More recently, membrane-integrated approaches have been proposed. Wagh *et al.*[39] designed self-standing PEMAC@NDCN membrane catalysts by covalently crosslinking nitrogen-deficient carbon nitride nanotubes (NDCN) with supramolecular polymer PEMAC. The catalyst achieved ORR $E_{1/2}$ = 0.87 V, OER potential = 1.48 V at 10 mA cm^{-2} (ΔE = 0.61 V, one of the lowest reported), and enabled FZABs to operate stably between −40 and 70 °C. The membrane also exhibited 0.34 MPa tensile without failure after 1000 bends. However, more than 1000 bending cycles caused interfacial peeling, raising electron-transfer resistance by 30%. In addition, the high precision required for regulating N defects in NDCN (error <0.5%) increased costs, and electrolyte ionic conductivity at −40 °C was only 1.2 mS cm^{-1}, limiting low-temperature power output. Among various modification strategies, nonmetallic boron doping has attracted considerable attention. The incorporation of boron into transition metal catalysts can effectively regulate the electronic structure, optimize the adsorption and desorption behaviour of key reaction intermediates, and thus enhance catalytic activity. Boron-induced modulation of active sites has been demonstrated to accelerate reaction kinetics and improve the overall performance of FZAB cathodes.

To address the dual bottlenecks of sluggish ORR kinetics and inadequate mechanical resilience in FZABs, while filling the gap of bimetallic borides being unexplored in flexible systems, this study develops a Ni–Fe–B catalyst with a nanocrystalline-amorphous composite structure *via* a two-step chemical reduction route. Leveraging the synergistic effects of the amorphous Ni–B matrix (abundant unsaturated sites and flexibility), uniformly dispersed Fe nanocrystals (enhanced electronic synergy), and mesoporous architecture (efficient mass transport), this design simultaneously boosts ORR activity and mechanical tolerance. As the first demonstration of bimetallic borides in FZABs, this work delivers a high-performance cathode catalyst with superior power output and durability, and provides a scalable design strategy for advanced flexible energy storage devices.

Experimental section

Catalyst preparation

Materials. All chemical reagents used for catalyst synthesis, including potassium borohydride (98%), nickel chloride hexahydrate (99%), iron chloride hexahydrate (99%), potassium hydroxide (85%), and ethanol, were purchased

from Shanghai Yinen Chemical Co., Ltd. All reagents were of analytical grade and used without further purification. Unless otherwise stated, all experiments were carried out at ambient temperature.

Synthesis procedure. The Ni–Fe–B catalyst was synthesized *via* a room-temperature chemical reduction process, as illustrated in Fig. 1.[40] Initially, 1.3202 g of KOH and 5.506 g of KBH_4 were dissolved in deionized water to prepare 100 mL of a 1 mol L^{-1} aqueous solution (the concentration of KBH_4 in solution A is approximately 1 mol L^{-1}), which was stirred for 20 min (solution A). Separately, 6.0635 g of nickel chloride hexahydrate was dissolved in 50 mL of deionized water to obtain a 0.5 mol L^{-1} solution, which was stirred for 20 min (solution B). Solution A (10 mL) was then added dropwise into solution B at a rate of 60 mL h^{-1} under magnetic stirring. After complete addition, the mixture was stirred for an additional 1 h, followed by filtration and washing to yield a black precipitate. The precipitate was repeatedly rinsed with deionized water and anhydrous ethanol, and subsequently dried in a vacuum oven at 60 °C for 12 h to obtain the Ni–B precursor. Next, 6.8255 g of iron(III) chloride hexahydrate was dissolved in 50 mL of deionized water to prepare a 0.5 mol L^{-1} solution (solution C), which was stirred for 20 min. Subsequently, all the Ni–B precursor (1.875 g, 0.025 mol of Ni^{2+}) prepared in the first step was added into solution C. 10 mL of solution A was added dropwise at 60 mL h^{-1} under magnetic stirring. After complete addition, the reaction mixture was stirred for another 1 h. The resulting precipitate was collected, rinsed thoroughly, and dried to yield the Ni–Fe–B catalyst. To prepare catalysts with different Ni/Fe molar ratios (1:1, 1:2, 2:1, 1:3, 3:1), 50 mL of 0.5 mol L^{-1} solution B ($NiCl_2 \cdot 6H_2O$, containing 0.025 mol Ni^{2+}) was used to prepare the Ni–B precursor, which was fully collected. The required amount of 0.5 mol L^{-1} solution C ($FeCl_3 \cdot 6H_2O$) was then added according to the target Ni/Fe molar ratio, thereby ensuring accurate control of the metal composition.[41]

Electrolyte gel. 18 g of potassium hydroxide was dissolved in 26 mL of deionized water and stirred for 1 h until the solution was cooled to room temperature (solution D). Subsequently, 3 g of acrylic acid and 0.5 g of *N,N'*-methylenebisacrylamide were added to solution D and stirred for another 1 h. The mixture was filtered through 15 cm qualitative filter paper in accordance with GB/T 1914-2007 to obtain the filtrate (solution E). Separately, 0.25 g of ammonium persulfate was dissolved in 5 mL of

Fig. 1 Synthesis procedure of Ni–Fe–B catalyst.

deionized water (solution F). Solution E was transferred to a Petri dish, and solution F was added dropwise under magnetic stirring until gelation occurred. The resulting hydrogel was then placed at 4 °C for 5 h to complete the preparation.[42]

Electrode preparation. The air cathode of the ZAB consisted of a gas diffusion layer, an active catalyst layer, and a current collector made of fine copper mesh. Catalyst powder (5 mg), acetylene black (1.7 mg, Zhengzhou Jinghong New Energy Technology Co., Ltd.), and PTFE solution (5 mg, Guangdong Jinde New Energy Technology Co., Ltd.) were dispersed in anhydrous ethanol and ultrasonicated for 20 min to obtain homogeneous slurry. The slurry was uniformly coated onto a 1 cm × 1 cm gas diffusion layer and dried in a vacuum oven at 60 °C for 4 h. The coated diffusion layer and copper mesh were then pressed together at 8 MPa to form a sheet with a thickness of 0.6 mm, completing the three-layer cathode. The anode was prepared from high-purity zinc sheets with a thickness of 0.02 mm (Haoyu Metal Materials Trading Co., Ltd.).

Catalyst characterization. The crystal structure was characterized using a PANalytical Empyrean X-ray diffractometer with Cu Kα radiation (λ = 0.15406 nm) operated at 40 kV and 40 mA. Data were collected over a 2θ range of 30–120° with a step size of 0.0167°, employing a 0.25° evanescent slit and a 0.04° solara slit. Surface morphology was examined using a Zeiss Sigma 300 field-emission scanning electron microscope in Inlens secondary electron mode at 5 kV. Samples were mounted on conductive adhesive and coated with a thin Au layer by sputtering for 60 s prior to imaging. Microstructural features were analyzed using a JEOL JEM-2100F high-resolution transmission electron microscope operated at 200 kV. Samples were ultrasonically dispersed in anhydrous ethanol, drop-cast onto a copper grid, and dried before observation. The specific surface area and pore size distribution were determined using a Quantachrome Autosorb-IQ analyzer after degassing at 120 °C for 7 h. The surface chemical composition was investigated by X-ray photoelectron spectroscopy (XPS, Thermo Fisher Nexsa) with a monochromatic Al Kα source operated at 15 kV and 10 mA under a vacuum of 5×10^{-10} Pa. Survey spectra were recorded with a pass energy of 50 eV, and binding energies were calibrated to the C 1s peak at 284.8 eV.

Electrochemical testing and FZAB. The electrochemical activity for ORR was evaluated in a standard three-electrode cell using a Hg/HgO reference electrode and a platinum counter electrode, connected to an electrochemical workstation (CHI 650, Shanghai Huachen). Catalyst ink was prepared by dispersing 200 mg of cathode catalyst in 10 mL deionized water and 100 μL polyethylene solution, followed by ultrasonication for 15 min. The slurry was uniformly brush-coated onto nickel foam at intervals of 3 minutes, followed by drying in a vacuum oven at 60 °C for 4 hours. The working electrode was tested in 150 mL of 1 mol L^{-1} KOH electrolyte. Cyclic voltammetry was carried out in the potential range of −1.0 to 1.0 V vs. Hg/HgO at a scan rate of

10 mV s^{-1}. Electrochemical impedance spectroscopy was conducted with a 5 mV AC perturbation in the frequency range of 100 kHz to 0.01 Hz. Stability tests of assembled FZABs were performed at a current density of 100 mA cm^{-2} with a cathode catalyst loading of 10 mg cm^{-2}. The gel electrolyte remained stable throughout the tests. Battery performance was further evaluated using a Neware testing system (Xiamen Tmax) at 25 °C. The FZAB consisted of an Ni–Fe–B cathode catalyst and a high-purity zinc flake anode.

Results and discussion

The crystal structure of the catalyst was characterized by XRD and TEM.[41] As shown in Fig. 2a, the XRD pattern exhibited no sharp diffraction peaks but only a broad feature between 20° and 30°, indicating an amorphous nature. Fig. 2b presents HRTEM images where lattice fringes with d = 0.20 nm, indexed to the α-Fe (110) plane, can be clearly observed in the Fe nanocrystal region, while the adjacent Ni–B matrix shows no ordered fringes, confirming its amorphous nature. The abrupt termination of Fe lattice fringes at the interface provides direct visual evidence of a crystalline-amorphous boundary. To aid visibility, arrows have been added to highlight this boundary. Consistent with these results, STEM contrast shows bright Fe nanocrystals embedded in a darker amorphous Ni–B background, confirming the structural distinction. Together with the XPS analysis revealing mixed Fe^{2+}/Fe^{3+} states, these results establish robust evidence for the coexistence of Fe nanocrystals and the amorphous Ni–B matrix.[43–45] These results suggest that the material adopts a
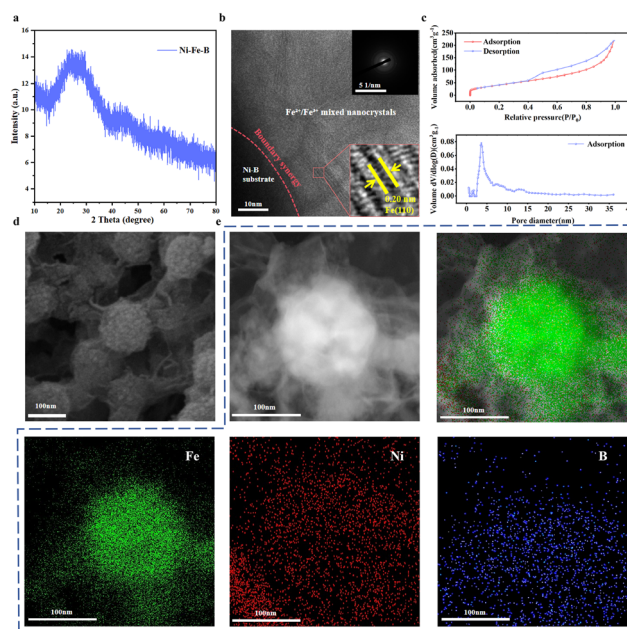

Fig. 2 (a) XRD pattern of Ni–Fe–B cathodic catalyst. (b) TEM image and SAED pattern of Ni–Fe–B cathodic catalyst. (c) Nitrogen adsorption–desorption isotherms and pore size distribution of Ni–Fe–B cathodic catalyst. (d) SEM image of Ni–Fe–B. (e) STEM image and elemental mappings.

hybrid state composed of microcrystalline and amorphous phases with short-range order and long-range disorder. In Fig. 2b and e, STEM and HRTEM images provide direct evidence of the nanocrystalline-amorphous composite structure. The Fe nanocrystals display clear lattice fringes (d = 0.20 nm, indexed to the (110) plane of α-Fe), while the surrounding Ni–B matrix shows no ordered fringes, consistent with an amorphous phase. The corresponding SAED pattern exhibits diffuse halo rings characteristic of amorphous Ni–B, along with faint diffraction spots arising from Fe nanocrystals. Furthermore, STEM observations indicate that the Fe nanocrystals are uniformly distributed with sizes ranging from ~10 to 50 nm, with the majority between 20 and 35 nm. These results confirm that the catalyst consists of nanocrystalline Fe domains embedded within an amorphous Ni–B matrix.

The amorphous character can be attributed to the rapid reduction environment during synthesis. In the preparation of the Ni–B precursor, KBH_4 acts as a strong reducing agent, and the controlled liquid-phase reduction of Ni^{2+} ions accelerates atomic diffusion relative to ordered nucleation, suppressing long-range crystallization and yielding an amorphous Ni–B alloy. Subsequent Fe doping introduces additional chemical disorders and promotes co-reduction of Ni^{2+} and Fe^{3+}, resulting in a nanocrystalline-amorphous composite. The smaller atomic radius of B compared to Ni and Fe, together with strong B–Ni and B–Fe covalent bonding, further stabilizes the amorphous matrix. Notably, the two-step chemical reduction route was specifically chosen for its ability to precisely tailor this nanocrystalline-amorphous structure-unlike high-temperature pyrolysis or one-step co-reduction, it avoids Fe nanocrystal agglomeration and preserves the amorphous Ni–B matrix, ensuring uniform bimetallic dispersion and interfacial synergy.

This amorphous structure is advantageous for catalytic applications in FZAB air cathodes. The random atomic configuration generates abundant unsaturated coordination sites, while short-range order produces surface defects such as grain boundaries, providing numerous active sites for ORR. Uniform distribution of Ni and Fe within the amorphous matrix induces electronic coupling, modifies the electron density of active sites, and optimizes oxygen adsorption–desorption kinetics. Hybridization of Ni and Fe d orbitals lowers the energy barrier for ORR intermediates (*e.g.*, OOH^-), thereby enhancing catalytic activity. The atomic-level uniform mixing obtained *via* solution reduction in the amorphous structure mitigates the typical phase separation problems encountered in conventional crystalline materials. Moreover, the homogeneous atomic-level mixing achieved in the amorphous phase prevents phase separation, ensuring long-term retention of active components and improved cycling stability.

Nitrogen adsorption–desorption analysis confirmed a mesoporous structure. As shown in Fig. 2c, the isotherm corresponds to a type IV profile with an H3-type hysteresis loop, characteristic of mesoporous networks formed by particle aggregation. The BET specific surface area was 155 m^2 g^{-1}, with an average pore size of 3.6 nm predominantly distributed in the 2–6 nm range, features that promote oxygen diffusion and adsorption[46] arises from the disordered atomic arrangement within the amorphous Ni–B matrix and the distribution of Fe nanocrystal particles. These structures provide numerous active surface sites and enhance gas diffusion pathways, promoting the adsorption and transport of oxygen molecules.[47]

SEM (Fig. 2d) and STEM images with elemental mapping (Fig. 2e) further demonstrated that Fe nanoparticles (10–50 nm) are uniformly dispersed within the Ni–B amorphous matrix, forming a nanocrystalline-amorphous composite. The Fe particles exhibited clear lattice contrast, while Ni and B remained homogeneously distributed without visible segregation, consistent with the two-step reduction mechanism: initial formation of an amorphous Ni–B precursor, followed by heterogeneous nucleation of Fe nanoparticles on the Ni–B surface and in solution.

The chemical states and electronic interactions of the Ni–Fe–B catalyst were investigated by XPS. As shown in Fig. 3a, the Ni 2p spectrum of the Ni–B precursor exhibited peaks at 855.5 eV ($2p_{3/2}$) and 873.3 eV ($2p_{1/2}$), corresponding to Ni^{2+} species in NiO or $Ni(OH)_2$. Fig. 3b shows the Ni 2p spectrum of the Ni–Fe–B catalyst, with characteristic peaks located at 856.48 eV and 873.7 eV, together with corresponding satellite peaks. The fitting results confirm the presence of surface-oxidized Ni^{2+} species.[48–50] In addition to these qualitative features, peak-area integration indicates that the fraction of Ni^{2+} at 856.48 eV in Ni–Fe–B increases by approximately 12% relative to Ni–B, whereas the satellite peak intensity decreases by about 18%. These variations suggest a reduction in the Ni electron cloud density, consistent with electron transfer toward Fe or B.

The Fe 2p spectrum of Fe–B (Fig. 3c) displayed peaks at 711.7 eV ($2p_{3/2}$) and 725.8 eV ($2p_{1/2}$), characteristic of Fe^{3+} species such as FeOOH or Fe_2O_3. In Ni–Fe–B, the Fe $2p_{3/2}$ peak shifted to lower binding energy (712.1 eV, Fig. 3d), suggesting partial reduction of Fe^{3+} to Fe^{2+} due to electron transfer from the Ni–B matrix. Quantitatively, fitting of the Fe 2p spectrum reveals an Fe^{2+} fraction of ~35% in Ni–Fe–B, in
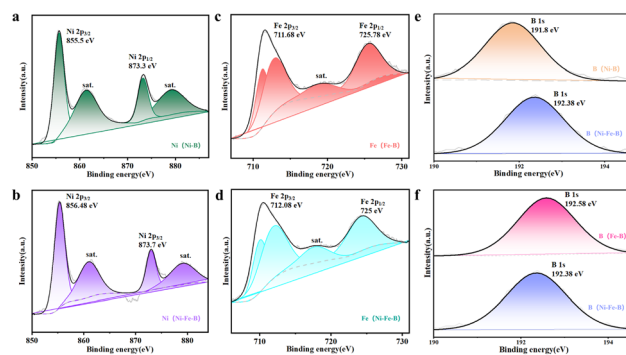

Fig. 3 XPS patterns of (a) Ni(Ni–B), (b) Ni(Ni–Fe–B), (c) Fe(Fe–B), (d) Fe(Ni–Fe–B), (e) B(Ni–B), B(Ni–Fe–B) and (f) B(Fe–B), B(Ni–Fe–B).

This journal is © The Royal Society of Chemistry 2026

*Catal. Sci. Technol.*, 2026, **16**, 1411–1420 | **1415**

contrast to 0% in Fe–B, confirming that B-mediated electron transfer from Ni facilitates Fe^{3+} reduction.[51]

Similarly, the B 1s spectrum of Ni–Fe–B (192.4 eV; Fig. 3e and f) lies between that of Ni–B (191.8 eV) and Fe–B (192.6 eV), confirming that B atoms coordinate with both Ni and Fe. Integration further demonstrates a 15% narrowing of the peak half-width and a 9% increase in the relative area fraction, indicating a more localized electron distribution after B coordination with the bimetallic centre. To further clarify the spectral assignments, it should be noted that the Ni 2p peaks at 710.8 eV ($2p_{3/2}$) and 724.5 eV ($2p_{1/2}$) with their corresponding satellites are consistent with standard Ni^{2+} species in NiO, confirming the presence of surface-oxidized Ni. Although Fe incorporation could, in principle, influence Ni binding energies, the relatively low Fe content (10 at%) and the absence of abnormal broadening or shifting in the Fe 2p spectrum suggest that the observed Ni 2p shift primarily arises from surface oxidation rather than Fe doping. In addition, the intermediate B 1s peak near 188.6 eV lies between the positions of Ni–B and Fe–B bonds, and the fitted Ni–B/Fe–B area ratio (9:1) matches the actual Ni:Fe atomic ratio. This observation is consistent with the STEM results showing Fe nanocrystals uniformly dispersed within the Ni–B matrix, further supporting the interpretation that B atoms coordinate with both Ni and Fe in the composite catalyst.

Taking together, these qualitative and quantitative XPS results demonstrate that incorporation of B regulates the Ni and Fe electronic structures, enhances electronic coupling between the amorphous Ni–B matrix and Fe nanocrystals, and optimizes intermediate adsorption. This "B-mediated electronic coupling" mechanism provides an atomistic explanation for the superior catalytic performance and cycling stability observed in flexible Zn-air batteries.[52] Although this work evaluated only representative Ni/Fe ratios, the observed trends provide sufficient evidence of composition–structure–performance correlations. A systematic exploration of a broader range of Ni/Fe ratios, including detailed analysis of the amorphous structure and chemical environment, is beyond the current scope but will be considered in future studies to further clarify the structure–activity relationships.

The laboratory FZAB was assembled using an air cathode, a solid electrolyte, and a zinc plate anode. The air cathode consisted of a gas diffusion layer, a catalyst layer, and a copper mesh current collector, while the anode employed high-purity zinc plates. A potassium hydroxide gel served as the electrolyte (Fig. 4a). The operating principle is based on coupled electrochemical reactions between the electrodes (Fig. 4b): zinc undergoes oxidation at the anode to form zincate ions with electron release, while oxygen diffuses through the gas diffusion layer to the catalyst surface, where it is reduced to hydroxide ions *via* a four-electron pathway. The overall reaction can be expressed as:

$$Zn + 4OH^- \rightarrow Zn(OH)_4^{2-} + 2e^- \qquad (R1)$$
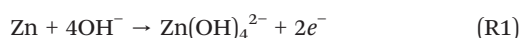
Electrons are conveyed through the external circuit to the air cathode, facilitating the oxygen reduction reaction (ORR) at the catalyst active layer's surface. The gas diffusion layer enables the movement of oxygen molecules to the catalyst active sites, resulting in the generation of hydroxide ions *via* a four-electron transfer pathway, as illustrated by the subsequent reaction equation:

$$O_2 + 2H_2O + 4e^- \rightarrow 4OH^- \qquad (R2)$$

The overall reaction equations for the anode and cathode are as follows:

$$2Zn + O_2 \rightarrow 2ZnO. \qquad (R3)$$

Prior studies on boride ORR catalysts have shown RRDE-verified four-electron selectivity in alkaline electrolytes (Fe_2B/rGO; amorphous boride systems), providing a relevant precedent for $4e^-$ ORR on B-containing transition-metal frameworks.[53,54] The optimized Ni–Fe–B cathode exhibited superior performance compared to Ni–B and Fe–B counterparts.

The optimized Ni–Fe–B cathode shows superior performance compared to Ni–B and Fe–B counterparts. Polarization curve measurements (Fig. 4c) reveal that at the optimized Ni/Fe molar ratio of 1:1, it achieves a peak power density of 224.9 mW cm^{-2} and an open-circuit voltage of 1.23 V, significantly outperforming the control samples. Cyclic voltammetry (CV) tests (Fig. 4d) further confirm that the redox peak current scales proportionally with the scan rate, indicating that the electrode reaction is primarily governed by surface adsorption behavior. This characteristic is closely related to the nanocrystalline-amorphous composite structure of the Ni–Fe–B catalyst. Specifically, Fe nanocrystals uniformly embedded in the Ni–B matrix not only serve as efficient active centers to enhance the adsorption of oxygen intermediates (OOH^-/OH^-)[55–57] but also cooperate with the amorphous Ni–B
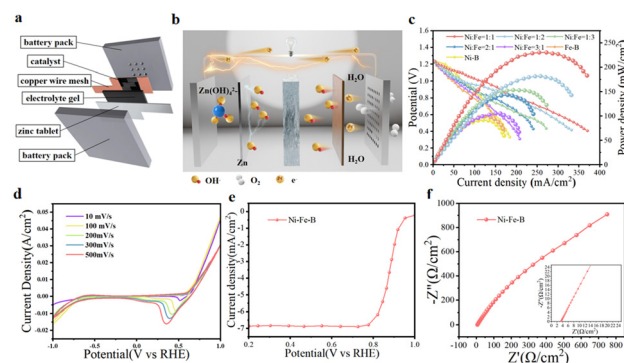

Fig. 4 (a) Schematic diagram of the FZAB structure. (b) Electrochemical reaction mechanism of FZAB. (c) Power density curves of Ni–Fe–B and related catalysts. (d) Cyclic voltammetry (CV) curves of Ni–Fe–B at different scan rates. (e) LSV curve of Ni–Fe–B catalyst. (f) EIS plots of Ni–Fe–B catalyst.

1416 | *Catal. Sci. Technol.*, 2026, **16**, 1411–1420

This journal is © The Royal Society of Chemistry 2026

matrix to form a continuous reaction interface. Meanwhile, the inherent mesoporous nature of the composite structure expands the electrochemically active region, enabling more active sites to participate in the reaction and establishing a structural foundation for efficient oxygen reduction.

The intrinsic ORR activity of the Ni–Fe–B catalyst was evaluated by linear sweep voltammetry (LSV) (Fig. 4e). The LSV curve shows a half-wave potential of approximately 0.86 V *vs.* RHE, which is comparable to that of commercial noble-metal catalysts and superior to most reported bimetallic boride-based ORR catalysts. This excellent performance originates from the synergistic modulation of the catalyst's structure on the ORR kinetics. On the one hand, Fe nanocrystals tailor the electronic structure of the Ni–B matrix, optimizing the adsorption energy of oxygen intermediates and reducing the energy barrier of the rate-determining step in the ORR process. On the other hand, the mesoporous channels within the composite structure facilitate the rapid diffusion of oxygen molecules and electrolyte ions, preventing the accumulation of intermediates on the catalyst surface. Together, these effects contribute to the efficient and stable ORR performance. Electrochemical impedance spectroscopy (EIS, Fig. 4f) analysis further reveals the interfacial electron transfer characteristics of the Ni–Fe–B catalyst. The abscissa of the intersection points between the high-frequency region of its Nyquist plot and the real axis is 3.4587 Ω cm^2, which corresponds to the solution resistance (R_s), this indicates low contact and ion transport resistance between the electrolyte and the electrode. Combined with the high-frequency magnified plot, the curve shows a short arc feature; the charge-transfer resistance (R_{ct}) is roughly estimated to be around 3–5 Ω cm^2, reflecting minimal resistance during the charge transfer process of the ORR on the electrode surface. The low R_{ct} value confirms that the "nanocrystalline-amorphous" composite structure of the Ni–Fe–B catalyst and the bimetallic electronic synergy effectively optimize the interfacial electron transfer efficiency, providing a kinetic guarantee for the rapid progression of the ORR. These results demonstrate that the catalyst possesses favorable catalytic activity and excellent reaction kinetic performance.[61,62]

In addition to high activity, durability is a critical criterion for evaluating the practical applicability of electrocatalysts in rechargeable batteries.[63] Catalysts that suffer from rapid degradation or unstable performance cannot meet the long-term operational demands of real devices. Therefore, in this work, we conducted extended cycling tests under constant current density to rigorously assess the long-term stability of our Ni–Fe–B catalyst, providing reliable evidence for its durability in practical applications. After assembly into a battery system, the long-term cycling performance of the Ni–Fe–B cathode was evaluated under galvanostatic charge–discharge conditions

at a current density of 100 mA cm^{-2} (Fig. 5a). The results showed that the device could operate stably for 100 h with minimal voltage decay (approximately 0.05 mV h^{-1}), confirming the excellent durability of the catalyst during extended cycling. Additionally, flexibility tests conducted at the same current density demonstrated that the cathode possessed outstanding mechanical tolerance: after repeated bending between 0° and 180°, only slight voltage fluctuations (<50 mV) were observed, and the charge–discharge polarization was negligible (Fig. 5b). The Ni–Fe–B catalyst developed in this study was systematically compared in performance with numerous cathode catalysts for flexible zinc-air batteries (FZABs) available in the market, including the commercial Pt/C catalyst. The results showed that the peak power density of commercial non-boride catalysts is typically only 120–160 mW cm^{-2}. As a traditional benchmark catalyst for the ORR, the commercial Pt/C catalyst also exhibits a peak power density of 175 mW cm^{-2} in flexible batteries. In contrast, the Ni–Fe–B catalyst in this study not only achieves a higher peak power density of 224.9 mW cm^{-2} but also demonstrates superior cycling stability (Table 1).[37,55,58–60,64,65] The enhanced durability of this catalyst originates from the anti-agglomeration property of its nanocrystalline-amorphous composite structure, which can effectively protect the active sites and simultaneously suppress the occurrence of side reactions such as zinc dendrite growth and hydrogen evolution.

The observed voltage stability can be attributed to the synergistic effect of the electrode structure, gel electrolyte, and gas diffusion layer. Specifically, the three-layer electrode structure (catalyst layer with polytetrafluoroethylene (PTFE) binder, gas diffusion layer, and copper mesh current collector) is pressed under a pressure of 8 MPa, which can ensure strong interfacial adhesion and prevent delamination, thereby maintaining continuous electron transport pathways. The KOH-based viscoelastic gel electrolyte can adapt to electrode deformation and maintain intimate contact with the catalyst layer, suppressing changes in ionic transport resistance. Meanwhile, the gas diffusion layer possesses both mechanical toughness and oxygen permeability, which can ensure a stable oxygen supply and avoid fluctuations in the kinetics of the ORR.

In terms of stability, Ni–Fe–B can continuously operate for 100 h at 100 mA cm^{-2}, whereas Pt/C shows about 20 h
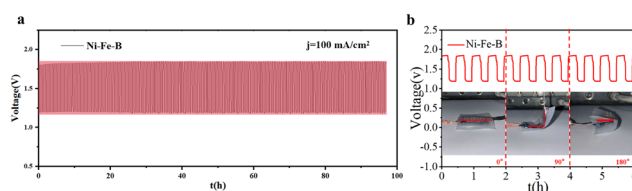

Fig. 5 (a) Charge–discharge cycling performance at a constant charge–discharge current density of 100 mA cm^{-2}. (b) Charge–discharge cycling performance testing at different folding angles with a constant charge–discharge current density of 10 mA cm^{-2}.

This journal is © The Royal Society of Chemistry 2026

Catal. Sci. Technol., 2026, **16**, 1411–1420 | 1417

Table 1 Performance comparison of Ni–Fe–B with representative non-precious metal catalysts and Pt/C in Zn-air batteries

Catalyst	Peak power density (mW cm^{-2})	Stability at 100 mA cm^{-2} (h)	Half-wave potential (V vs. RHE)	Ref.
Ni–Fe–B	224.9	100	0.86	This work
CoFe@NC/CC	—	16	—	58
Mn$_1$/NDC	—	645 cycles	—	59
Fe$_{3\%}$Co$_{3\%}$Ni$_{9\%}$-NC1000	291.2	200	0.927	60
FeCo-NC	200	190	0.877	55
20 wt% Pt/C + IrO$_2$	64.2	50	—	58
20 wt% Pt/C + RuO$_2$	159.3	35	—	58
Fe$_3$C/MnO-NC	96.54	48	0.86	37
Co–N$_x$/EPCF	81	115	0.82	38
PEMAC@NDCN	211	37	0.87	39
Pt/C (commercial)	175	20	0.867	42

under similar conditions, indicating that Ni–Fe–B possesses a notable durability advantage in Zn-air battery operation.[66] In addition to Pt/C, Table 1 also lists representative non-noble metal catalysts under similar testing conditions. Besides, Raikova et al. employed carbon-free nickel cobaltite air electrodes for rechargeable ZABs, focusing on bifunctional ORR reversibility and long-term cycling; such oxide systems typically deliver medium-to-high device power with robust charge–discharge stability. Sonoo et al. investigated N-/Fe–N-doped carbons in near-neutral Zn-air cells, where milder electrolytes usually lead to moderate ORR half-wave potentials and moderate-to-lower power output but good durability. Sun et al. reported ordered PdZn alloys, which offer high intrinsic ORR activity (high $E_{1/2}$) at the expense of noble-metal content. Compared with these reports, our Ni–Fe–B (non-noble) catalyst in a flexible Zn-air configuration achieves a relatively high peak power density and excellent 100 h discharge stability, indicating a competitive activity–durability balance among cost-effective cathodes for Zn-air batteries. Meanwhile, its intrinsic ORR metric ($E_{1/2} \approx 0.86$ V vs. RHE) is comparable to state-of-the-art non-noble systems under alkaline conditions, while offering the added advantages of mechanical flexibility and strong interfacial adhesion.[67–69] These comparative results provide a clear benchmark and place the performance of Ni–Fe–B in the broader context of both noble-metal and non-noble-metal catalysts.

In summary, these features collectively construct a highly active and stable ORR interface, which has strong nanocrystalline-amorphous electronic coupling, efficient mesoporous mass transfer capability, and kinetic optimization characteristics. It not only outperforms commercial Pt/C and most non-boride catalysts in performance but also can meet the mechanical requirements of flexible devices, laying a solid foundation for the development of wide-temperature flexible zinc-air batteries with strong adaptability and excellent durability. In future work, density functional theory (DFT) calculations and synchrotron-based characterization could be combined with experimental studies to gain deeper insights into the intrinsic catalytic mechanisms at the nanocrystalline-

amorphous interface. Such advanced analyses could help identify the active sites, clarify the reaction pathways, and guide rational structural optimization, thereby facilitating the development of high-performance flexible Zn-air batteries for practical applications.

Conclusions

In summary, a Ni–Fe–B catalyst with a nanocrystalline-amorphous composite structure was successfully synthesized through a two-step chemical reduction method. The amorphous Ni–B matrix coupled with Fe nanocrystals generates abundant active sites, efficient mass transport pathways, and favourable electronic modulation, which together accelerate ORR kinetics. When applied in flexible zinc–air batteries, the catalyst achieved a peak power density of 224.9 mW cm^{-2}, and remarkable durability with a voltage decay rate of only 0.05 mV h^{-1} over 100 h. Furthermore, the device maintained stable operation under repeated 0–180° bending cycles, with voltage fluctuations below 50 mV. These findings highlight the unique advantages of borides in integrating structural stability, electronic synergy, and mechanical adaptability, and provide a promising strategy for advancing next-generation flexible energy storage systems.

Author contributions

Sai Li: conceptualization, funding acquisition, supervision. Shuoshuo Wang: data curation, formal analysis, writing – original draft. Qinqin Chen: formal analysis, investigation. Dongyuan Yang: funding acquisition, supervision. Yuhang Wang: formal analysis, methodology. Haixia Wu: methodology. Yameng Ma: methodology. Zekai Ma: methodology. Qi Chen: software. Jiahao Zhouhuang: software. Qiuliang Yu: resources. Lihui Zeng: resources. Haiyan Zhu: formal analysis. Peng Ren: funding acquisition, resources. Qing Feng: funding acquisition, resources. Rui Tan: supervision, writing – review & editing. Zhiming Feng: formal analysis, supervision, writing – review & editing.

1418 | Catal. Sci. Technol., 2026, 16, 1411–1420

This journal is © The Royal Society of Chemistry 2026

Conflicts of interest

The authors declare that they have no known competing financial interests or personal relationships that could have appeared to influence the work reported in this paper.

Data availability

The data supporting the findings of this study are available from the corresponding author upon reasonable request.

Acknowledgements

Notes and references

1 N. Liu, D. Liu, Y. Zhan, Q. Chen, Y. Qiao and R. Tan, *eScience*, 2025, **1**, e70008.

2 Z. Feng, J. Huang, S. Jin, G. Wang and Y. Chen, *J. Power Sources*, 2022, **520**, 230808.

3 G. Liao, S. Li, Y. Luo, Z. Xin, Q. Li, R. Tan, K. Zhang and Z. Feng, *J. Alloys Compd.*, 2025, **1013**, 178599.

4 Z. Feng, S. Zheng, H. Che and Z. Gao, *J. Alloys Compd.*, 2025, **1044**, 184360.

5 Q. Liu, T. Fu, H. Xiao, Y. Yu, Z. Che, Y. Zhang, A. Chen, M. Li and T. Liu, *Carbon Neutralization*, 2025, **4**, e70024.

6 Y. Zhao, L. Yang, Y. Long, M. Xi, A. Chen and H. Zhang, *J. Energy Chem.*, 2024, **95**, 490–498.

7 X. Song, L. Sun, P. Gao, R. Cui, W. Han, X. Huang and Z. Tang, *EcoEnergy*, 2025, **3**, e70011.

8 Y. Zhao, R. Tan, J. Yang, K. Wang, R. Gao, D. Liu, Y. Liu, J. Yang and F. Pan, *J. Power Sources*, 2017, **340**, 160–166.

9 L. Zhuang, W.-B. Cai, H.-X. Ji, Q. Li, G.-W. Wang, S. Xin, Q. Zhao, F.-Y. Cheng, Y.-G. Guo and L.-Q. Mao, *Dianhuaxue*, 2025, **31**, 3.

10 Y. Luo, Y. Qiao, H. He, M. Chen, G. Liu, X. Liu, L. Pan, Z. Feng and R. Tan, *J. Power Sources*, 2025, **631**, 236297.

11 S. Zheng, Z. Feng, Y. Lu, Y. Hua and Z. Gao, *Mater. Today Commun.*, 2025, **45**, 112242.

12 F. Zhan, L. Huang, Y. Luo, M. Chen, R. Tan, X. Liu, G. Liu and Z. Feng, *J. Mater. Sci.*, 2025, **60**, 2199–2223.

13 Z. Feng, Y. Luo, D. Li, J. Pan, R. Tan and Y. Chen, *Chain*, 2025, **2**, 1–14.

14 Y.-R. Liu, M. Zhang, Y.-H. Yu, Y.-L. Liu, J. Li, X.-D. Shi, Z.-Y. Kang, D.-X. Wu, P. Rao, Y. Liang and X.-L. Tian, *Dianhuaxue*, 2025, **31**, 2504132.

15 N. Liu, Y. Zhan, R. Tan, G. Zhao and J. Song, *Chain*, 2025, **2**, 211–226.

16 D. Li, S. Xie, J. Liang, B. Ma, J. Fu, J. Wu, Y. Feng and Z. Feng, *Sep. Purif. Technol.*, 2024, **340**, 126545.

17 M. Tang, X. Zou, L. Wu, G. Liu, R. Chen and L. An, *Mater. Rep.: Energy*, 2025, 100376.

18 J. Liu, S. Xie, D. Li, Z. Feng, H. Lu, X. Li, J. Liang, B. Ma, J. Fu, J. Xie, X. Zhi and Y. Feng, *Appl. Catal., B*, 2025, **379**, 125700.

19 D. Li, J. Liu, X. Chen, Z. Feng, S. Wang, Y. Wang, N. Lin, J. Wu and Y. Feng, *Appl. Catal., B*, 2025, **365**, 124824.

20 S. Li, Z. Xin, Y. Luo, G. Liao, Q. Li, K. Zhang, Z. Tehrani, R. Tan and Z. Feng, *Ionics*, 2025, **31**, 4591–4602.

21 Z. Feng, G. Gupta and M. Mamlouk, *J. Appl. Polym. Sci.*, 2024, **141**, e55340.

22 C. Wang, Z. Feng, Y. Zhao, X. Li, W. Li, X. Xie, S. Wang and H. Hou, *Int. J. Hydrogen Energy*, 2017, **42**, 29988–29994.

23 Z. Feng, G. Gupta and M. Mamlouk, *Int. J. Hydrogen Energy*, 2023, **48**, 25830–25858.

24 M. Zhang and N. Garcia-Araez, *Electrochim. Acta*, 2024, **499**, 144686.

25 F. Chen, F. Yang, H. Chu, J. Xu, K. Yang, J. D. Akoto, A. Haider, X. Wang, J. Yang, X. Liu, Z. Feng and R. Tan, *Battery Energy*, 2025, e70050, DOI: 10.1002/bte2.20250043.

26 N. Vangapally, T. R. Penki, Y. Elias, S. Muduli, S. Maddukuri, S. Luski, D. Aurbach and S. K. Martha, *J. Power Sources*, 2023, **579**, 233312.

27 X. Liu, X. Tian, H. Zhang, Y. Gan, H. Hao, Y. Luo, Z. Feng, Y. Qiao, Z. Jiang, X. Zhu, C. Wang, M. Larimi, Y. Zhao, C. Ye, R. Tan and J. Yang, *Rare Met.*, 2025, 1–34.

28 V. Jose, J. M. V. Nsanzimana, H. Hu, J. Choi, X. Wang and J. M. Lee, *Adv. Energy Mater.*, 2021, **11**, 2100157.

29 Y. Zhu, D. Zheng, X. Xing, S. Wu, X. Guo, J. Liu, X. Guo, J. Zhou, Y. Jiao and B. Zeng, *J. Phys. Chem. C*, 2024, **128**, 7007–7025.

30 S. Zaman, L. Huang, A. I. Douka, H. Yang, B. You and B. Y. Xia, *Am. Ethnol.*, 2021, **133**, 17976–17996.

31 Z. Lu, G. Li, K. Sheng, T. Wu, W. Luo, H. Zhou and Q. Yi, *J. Alloys Compd.*, 2025, **1039**, 183119.

32 T. Lu, N. Xu, B. Zhou, L. Guo, X. Wen, S. Lou, G. Liu, W. Yang, N. Yang and M. Safari, *eScience*, 2025, 100450.

33 B. Zhuang, N. Xu, X. Xu, L. Dai, Y. Wang, M. Wang, K. Wu and J. Qiao, *Mater. Rep.: Energy*, 2025, 100352.

34 Z. Wang, Y. Zhang, J. Zhang, N. Xu, T. Lu, B. Zhuang, G. Liu, W. Yang, H. Lei and B. Tian, *Chin. J. Catal.*, 2025, **73**, 311–321.

35 Q. Zhou, X. He, M. Min, M. Song, P. Wang, W. Huang and C. Xiong, *Composites, Part B*, 2025, **307**, 112877.

36 Q. Zhou, S. Cui, M. Song, X. He, L. Lu, D. Liu and C. Xiong, *Inorg. Chem.*, 2025, **64**, 2857–2867.

37 J. Zhong, Q. Xu, R. Li and D. Yuan, *Appl. Catal., B*, 2025, **361**, 124615.

38 Y. Zhang, J. Wang, M. Alfred, P. Lv, B. Liu and Q. Wei, *J. Power Sources*, 2022, **544**, 231865.

39 N. K. Wagh, S. S. Shinde, C. H. Lee, S.-H. Kim, D.-H. Kim, H.-D. Um, S. U. Lee and J.-H. Lee, *Nano-Micro Lett.*, 2022, **14**, 190.

This journal is © The Royal Society of Chemistry 2026

Catal. Sci. Technol., 2026, **16**, 1411–1420 | 1419

40 S. Li, Z. Xin, J. Han, Z. Feng, G. Liao, S. Wang, K. Liu, Q. Li, T. X. Liu and M. Bayati, *Ionics*, 2024, **30**, 7213–7222.

41 S. Li, G. Liao, D. Bildan, Z. Feng, H. Cai, J. Han, Z. Xin, K. Liu, Q. Li, J. Shang and T. X. Liu, *Int. J. Hydrogen Energy*, 2024, **67**, 448–457.

42 Y. He, H. Li, Y. Wang, Y. Jia, Y. Liu and Q. Tan, *J. Energy Chem.*, 2024, **90**, 610–620.

43 L. Zhang, W. Liu, W. Guo, J. Bao, X. Zhang, J. Liu, D. Wang, F. Meng and Z. Liu, *IEEE J. Photovolt.*, 2016, **6**, 604–610.

44 F. Li, T. Liu, J. Zhang, S. Shuang, Q. Wang, A. Wang, J. Wang and Y. Yang, *Mater. Today Adv.*, 2019, **4**, 100027.

45 Q. Xia, P. Ren and H. Meng, *J. Mater. Res. Technol.*, 2022, **18**, 4479–4485.

46 C. Ye, L. Zhang and Y. Shen, *ACS Mater. Lett.*, 2024, **6**, 2858–2887.

47 Y. Qian, X. Liu, X. Zheng, Z. Yang, Y. Yu, F. Gao, X. Guo, Y. Liu, X. Cao and R. Guo, *Chin. J. Chem.*, 2024, **42**, 2647–2655.

48 L. Cheng, Y. Li, J. Fan, M. Xie, X. Liu, P. Sun and X. Dong, *Sep. Purif. Technol.*, 2024, **333**, 125742.

49 W. Zhang, A. Ren, C. Pan and Z. Liu, *Int. J. Hydrogen Energy*, 2022, **47**, 30494–30502.

50 Y. Jin, M. Yu, E. Kan and C. Zhan, *J. Mater. Chem. A*, 2025, 24831.

51 V. Mihalache, C. Negrila, M. Secu, I. Mercioniu, N. Iacob and V. Kuncser, *Results Phys.*, 2023, **51**, 106644.

52 C. Guo and C. Wang, *Int. J. Hydrogen Energy*, 2024, **60**, 524–530.

53 X. Zhu, Y. Li, X. Tian, R. Wang, S. Wang, H. Wang, J. Yu and T. Huang, *Int. J. Hydrogen Energy*, 2023, **48**, 28354–28366.

54 S. Li, L. Shi, Y. Guo, J. Wang, D. Liu and S. Zhao, *Chem. Sci.*, 2024, **15**, 11188–11228.

55 Y. He, X. Yang, Y. Li, L. Liu, S. Guo, C. Shu, F. Liu, Y. Liu, Q. Tan and G. Wu, *ACS Catal.*, 2022, **12**, 1216–1227.

56 S. S. Patil, V. N. Narwade, F. U. Shaikh, R. S. Sonkawade, M.-L. Tsai, T. Hianik and M. D. Shirsat, *Microchem. J.*, 2025, 114267.

57 T. J. Shaldehi, S. Rowshanzamir, K. S. Exner, F. Viñes and F. Illas, *ACS Appl. Mater. Interfaces*, 2025, **17**, 6450.

58 S. Wang, M. Zhang, X. Mu, S. Liu, D. Wang and Z. Dai, *Energy Environ. Sci.*, 2024, **17**, 4847–4870.

59 Q. Liu, H. Shi, T. Han, L. Wang and H. Fu, *Energy Storage Mater.*, 2024, **67**, 103255.

60 W. Zhai, Y. He, Y.-E. Duan, S. Guo, Y. Chen, Z. Dai, L. Liu and Q. Tan, *Appl. Catal., B*, 2024, **342**, 123438.

61 Y. Luo, Y. Zhang, J. Zhu, X. Tian, G. Liu, Z. Feng, L. Pan, X. Liu, N. Han and R. Tan, *Small Methods*, 2024, **8**, 2400158.

62 Q. Zhou, M. Min, M. Song, S. Cui, N. Ding, M. Wang, S. Lei, C. Xiong and X. Peng, *Small*, 2024, **20**, 2307943.

63 Z. Feng, G. Gupta and M. Mamlouk, *RSC Adv.*, 2023, **13**, 20235–20242.

64 X. Lang, Z. Hu and C. Wang, *Chin. Chem. Lett.*, 2021, **32**, 999–1009.

65 Q. Wang, B. Chu, C. Shang, B. Shao, F. Yang, D. Dang, L. Li, M. Gu, X. Xiao and Q. Xu, *Adv. Mater.*, 2025, e14343.

66 J. Sun, M. Shen, A.-J. Chang, C. Liang, C. Xiong, C. Hou, J. Li, P. Wang, J. Li and J. Huang, *Chem. Eng. J.*, 2025, **503**, 158551.

67 G. Raikova, K. Krezhov, T. Malakova, E. Mihaylova-Dimitrova, P. Tzvetkov and B. Burdin, *Electrochim. Acta*, 2025, 146801.

68 M. Sonoo, T. K. Zakharchenko, M. Noked and R. R. Kapaev, *Electrochim. Acta*, 2025, 146662.

69 Z. Sun, S. Liu, Y. Guo, F. Zheng, B. Nan, W. Kang, K. Qu, L. Wang, R. Li, Z. Li, L. Dong and H. Li, *Electrochim. Acta*, 2024, **478**, 143857.

1420 | *Catal. Sci. Technol.*, 2026, **16**, 1411–1420

This journal is © The Royal Society of Chemistry 2026